Modulation of surface states in Sb_2Te_3/Bi_2Te_3 topological insulator heterostructures: The crucial role of the first adlayers

V. M. Pereira,[1] C. N. Wu,[1,2] L. H. Tjeng,[1] and S. G. Altendorf[1]
[1]*Max Planck Institute for Chemical Physics of Solids, Nöthnitzer Strasse 40, 01187 Dresden, Germany*
[2]*Department of Physics, National Tsing Hua University, Hsinchu 30013, Taiwan*

(Received 23 November 2020; revised 17 February 2021; accepted 1 March 2021; published 18 March 2021)

The hunt for an ideal topological insulator, where the Dirac point is situated in a desirable energetic position and the bulk remains insulating, has motivated experiments on band structure engineering in these materials. To achieve this, Sb_2Te_3 and Bi_2Te_3 are commonly combined in ternary compounds or, less frequently, in heterostructures. Here we report on the growth of Sb_2Te_3/Bi_2Te_3 heterostructures by means of molecular-beam epitaxy. Using angle-resolved photoelectron spectroscopy, we are able to differentiate between the shift of the chemical potential and the changes in the electronic structure, causing the lift-off of the Dirac point away from the bulk valence band when varying the Sb_2Te_3 adlayer thickness. Our paper demonstrates that the important modulation of the surface states takes place for the very first Sb_2Te_3 layers, while thicker adlayers only cause a gradual change of the bulk states and a rigid shift of the chemical potential. Furthermore, we observe the occurrence of diffusion between the Bi_2Te_3 and Sb_2Te_3 layers and conclude that a growth at room temperature, followed by annealing, maintains an acceptable crystalline quality while substantially reducing the interdiffusion.

DOI: 10.1103/PhysRevMaterials.5.034201

I. INTRODUCTION

In the recent topological insulator (TI) research, a great effort has been put into developing methods to tailor the band structure of the materials. The studies are motivated by the fact that an exposed Dirac point at (or close to) the Fermi level and an insulating behavior of the bulk are the key ingredients for a direct access of the exceptional properties of the topological surface states by transport measurements. Most materials, however, naturally do not have these characteristics. For three-dimensional TIs [1,2], as the prototypical Bi_2Se_3, Bi_2Te_3, and Sb_2Te_3 compounds, the bulk conductivity is often not zero due to doping caused by vacancies and antisite defects that shifts the Fermi level into the bulk conduction band (for Bi_2Se_3 and Bi_2Te_3) or into the bulk valence band (for Sb_2Te_3) [3–6]. For the same reason, the Dirac point usually does not lay directly at the Fermi level for Bi_2Se_3 and Sb_2Te_3 [3,7]. For Bi_2Te_3, it is furthermore buried in the bulk valence band [4,8].

A successful strategy to optimize the TIs is to combine these materials which share the same crystal structure with close lattice constants but have complementary electronic properties. This approach has been pursued by growing ternary or even quaternary TIs, as $(Bi_{1-x}Sb_x)_2Te_3$ or $(Bi_{1-x}Sb_x)_2(Te_{1-y}Se_y)_3$ [9–15]. By varying the composition, a charge compensation between electron and hole doping can be achieved, shifting the Fermi level into the bulk band gap and thus suppressing the bulk conductivity; and also the position of the Dirac point can be tuned.

An elegant alternative route is the combination of typically *n*- and *p*-type doped TIs in heterostructures. Here we focus on the very promising heterostructures consisting of Sb_2Te_3 and Bi_2Te_3 [16–19]. Since the materials have the same crystal structure and rely on van der Waals forces, the epitaxial growth of heterostructures is viable. Furthermore, no topological interface states should form due to the shared bulk $\mathbb{Z}_2$ topology [18,20]. Chang *et al.* [18] showed that a TI heterostructure with just one quintuple layer (QL) on top has the topological surface states already modified significantly. Eschbach *et al.* [17] studied heterostructures in which the thickness of the Sb_2Te_3 adlayer was varied from 6 to 25 QLs and observed a shift of the topological surface states. This shift of ≈200 meV is also accompanied by a transition from *n*- to *p*-type dominated transport. A theoretical study by Aramberri and Muñoz [20], on the other hand, predicts that the significant changes on the surface states happen mainly in the first three QLs of Sb_2Te_3, a thickness range that was not covered in these experimental studies.

In this paper, we therefore systematically study the evolution of the electronic structure of molecular-beam epitaxy-grown Sb_2Te_3/Bi_2Te_3 heterostructures from very thin (1 QL) to thick (40 QLs) Sb_2Te_3 adlayers, with focus on the thin layers for which we expect the largest effects on the surface states to occur. Using *in situ* angle-resolved photoelectron spectroscopy, we are able to distinguish two effects, namely, the modulation of the topological surface states and the shift of the chemical potential which determines the type and density of the charge carriers. We also investigate the extent of interdiffusion at the interface of the two TI layers for two

Published by the American Physical Society under the terms of the Creative Commons Attribution 4.0 International license. Further distribution of this work must maintain attribution to the author(s) and the published article's title, journal citation, and DOI. Open access publication funded by the Max Planck Society.

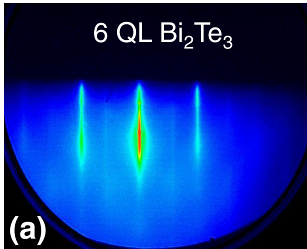

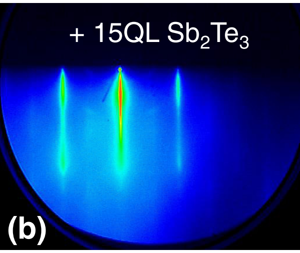

FIG. 1. RHEED patterns of (a) 6 QL Bi_2Te_3 on Al_2O_3 (0001) and (b) 15 QLs of Sb_2Te_3 grown on top.

alternative growth procedures and its influence on the electronic structure.

II. EXPERIMENT

The thin-film heterostructures were prepared by molecular-beam epitaxy (MBE) in an *in situ* system with base pressure of about 2×10^{-10} mbar. Epi-polished Al_2O_3 (0001) substrates were purchased from Crystec GmbH. Prior to the deposition, they were annealed at 600 °C for 2 h in an oxygen pressure of 1×10^{-6} mbar. High-purity Bi, Sb, and Te were coevaporated from effusion cells, and their flux rates were measured using a quartz crystal monitor at the growth position. Bulk insulating Bi_2Te_3 films were grown using a Te-distillation-assisted growth method in a two-step procedure following the recipes of Refs. [21–23]. The flux rates were set at 0.5 Å/min for Bi and at 1.6 Å/min for Te. First, 3 QLs of Bi_2Te_3 were deposited at a substrate temperature of 160 °C and annealed at 240 °C in Te atmosphere for 30 min. In the second step, subsequent QLs were deposited at 220 °C to achieve a nominal total thickness of 6 QLs of Bi_2Te_3 (≈6 nm). Subsequently, Sb_2Te_3 was deposited on top in the conditions specified in Sec. III below.

Reflection high-energy electron diffraction (RHEED) was used to monitor in *real time* the epitaxial growth, using a STAIB Instruments RH35 system with the kinetic energy of the electrons set at 15 keV. The samples were characterized *in situ* by x-ray photoelectron spectroscopy (XPS) using monochromatized Al K_α light (1486.6 eV) and angle-resolved photoelectron spectroscopy (ARPES) using a nonmonochromatic He discharge lamp with 21.2-eV photon energy (He I line) at room temperature and using a Scienta R3000 electron energy analyzer. The overall energy resolution was 0.35 eV for XPS and 0.1 eV for ARPES. The angular resolution was 1°, which corresponds to a momentum resolution of about 0.037 $Å^{-1}$. All ARPES spectra were measured along the $\bar{\Gamma} - \bar{K}$ direction.

III. RESULTS AND DISCUSSION

A. Sb_2Te_3/Bi_2Te_3 heterostructures grown at high temperature

Sb_2Te_3 films with thicknesses varying between 1 and 40 QLs were grown on top of 6 QLs of Bi_2Te_3. For the growth of the Sb_2Te_3 layer, the substrate temperature was kept at 220 °C and the flux rates were kept at ≈0.5 Å/min for Sb and at ≈1.6 Å/min for Te, following the Te distillation method also employed for the growth of Bi_2Te_3 [21–24].

Figures 1(a) and 1(b) show the RHEED patterns of 6 QL Bi_2Te_3 and 15 QL Sb_2Te_3 grown on top of it, respectively. The presence of well-defined streaks for both layers indicates the good crystalline quality of the films and an epitaxial growth of the Sb_2Te_3 adlayer.

ARPES was used to study the surface electronic structure of the heterostructures. Figures 2(a)–2(f) show the spectra close to the Fermi level for films with varying thickness of the upper Sb_2Te_3 layer. We can clearly observe the topological surface states as indicated by the blue dashed lines. Their crossing point determines the position of the Dirac point (see Appendix A for details). This position of the Dirac point visibly shifts to lower binding energies as the thickness of the Sb_2Te_3 layer increases, shifting from ≈175 meV below the Fermi level for 6 QL Bi_2Te_3 to ≈65 meV above the Fermi level for 15 QL Sb_2Te_3 + 6 QL Bi_2Te_3 and crossing the Fermi level for a thickness of ≈10 QL Sb_2Te_3. This behavior is summarized in Fig. 2(g). The highly tunable position of the Dirac point in relation to the Fermi level, by about 240 meV, and specifically the ability to precisely tune the Fermi level

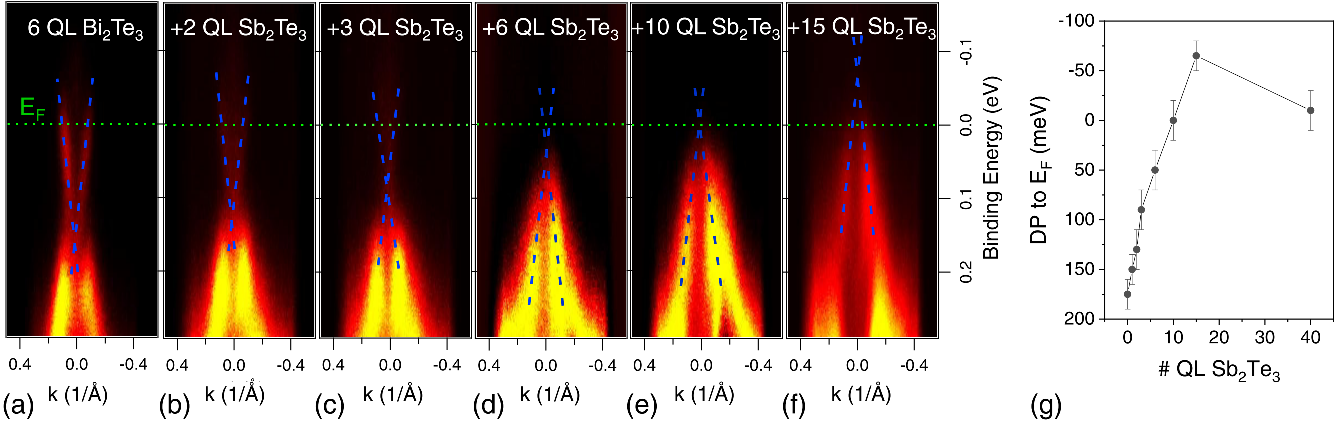

FIG. 2. ARPES results of Sb_2Te_3 grown on top of 6 QLs of Bi_2Te_3. From (a) to (f) the thickness of the top Sb_2Te_3 layer varies from 0, 2, 3, 6, 10, and 15 QLs, respectively. The green dashed line indicates the position of the Fermi level (E_F). The blue dashed lines indicate the positions of the topological surface states which were aligned with the maxima of the contour plots of the spectra. Their crossing represents the position of the Dirac point (DP). (g) Position of the Dirac point in relation to the Fermi level, varying with the thickness of the Sb_2Te_3 layer.

to the position of the Dirac point, is desirable for exploring the exotic quantum phenomena. This property has been previously reported for similar heterostructures [17]. However, one should note that two factors come into play in this result. On the one hand, the chemical potential varies with the thickness of the upper Sb_2Te_3 layer probably due to the presence of defects causing uncontrolled doping. On the other hand, the electronic structure alters. The Dirac point is lifted from the bulk valence band (as characteristic of Bi_2Te_3) into the bulk band gap (characteristic of Sb_2Te_3). To distinguish these two effects, overview ARPES spectra of all the samples were studied. Figure 3(a) shows such a spectrum with a wider energy range for a film with 10 QL Sb_2Te_3 grown on Bi_2Te_3. The energy distribution curves integrated over the area between the yellow lines are depicted in Fig. 3(b) for various thicknesses of the Sb_2Te_3 layer, as well as for a pure Bi_2Te_3 film. Here, one can identify two prominent and common features, marked as A (at ≈0.8–1.0-eV binding energy) and B (≈0.1–0.2 eV).

It is important to point out that—although ARPES is a very surface sensitive technique with a mean free path of only ≈0.5 nm [25], i.e., the measurement probes almost exclusively the topmost quintuple layer—the spectrum displays not only the surface state but also the bulk states since the latter are delocalized over the entire thickness of the heterostructure and are thus also present at the topmost quintuple layer. Since the surface state is observed as a Dirac cone close to the Fermi level for all the samples, we inevitably arrive at the conclusion that A and B are bulk states.

A closer inspection of the positions of these two features in relation to the Fermi level [Fig. 3(c)] shows that for pure Bi_2Te_3 and for the heterostructures with 1–3 QLs of Sb_2Te_3, the energies remain relatively constant (see Appendix B for details on the determination of the peak position). However, for thicker Sb_2Te_3 layers, the positions of A and B change significantly, with an overall trend similar to the one observed in Fig. 2(g). This shift of the entire band structure towards lower binding energies for increasing Sb_2Te_3 thickness can be attributed to a shift of the chemical potential. Thus, it is also quite susceptible to random defects that can affect the doping level of each sample. This, in turn, might explain the higher binding energies (in relation to E_F) of the 40 QL Sb_2Te_3 film.

In addition to the overall shift of the energy positions of A and B in relation to the Fermi level for thicker adlayers, a change of the relative distance between A and B can be noticed [Fig. 3(d)]. While the peaks are separated by ≈0.78 eV for the very thin Sb_2Te_3 adlayers of 1–3 QLs, the distance gradually decreases for increasing Sb_2Te_3 thickness in the intermediate thickness range, and reaches a minimum of ≈0.72 eV for thick Sb_2Te_3 layers of 15 QLs and more. This behavior can be understood as follows: For 1–3 QLs of Sb_2Te_3, no significant change in the separation of features A and B is observed, consistent with the fact that for the very thin Sb_2Te_3 adlayers the bulk electronic structure of the heterostructure is mainly governed by the thicker Bi_2Te_3 bottom layer. On the other end, for the thick Sb_2Te_3 adlayers of 15 QLs and more, the separation of A and B is also constant, but at a smaller value showing that now the character of

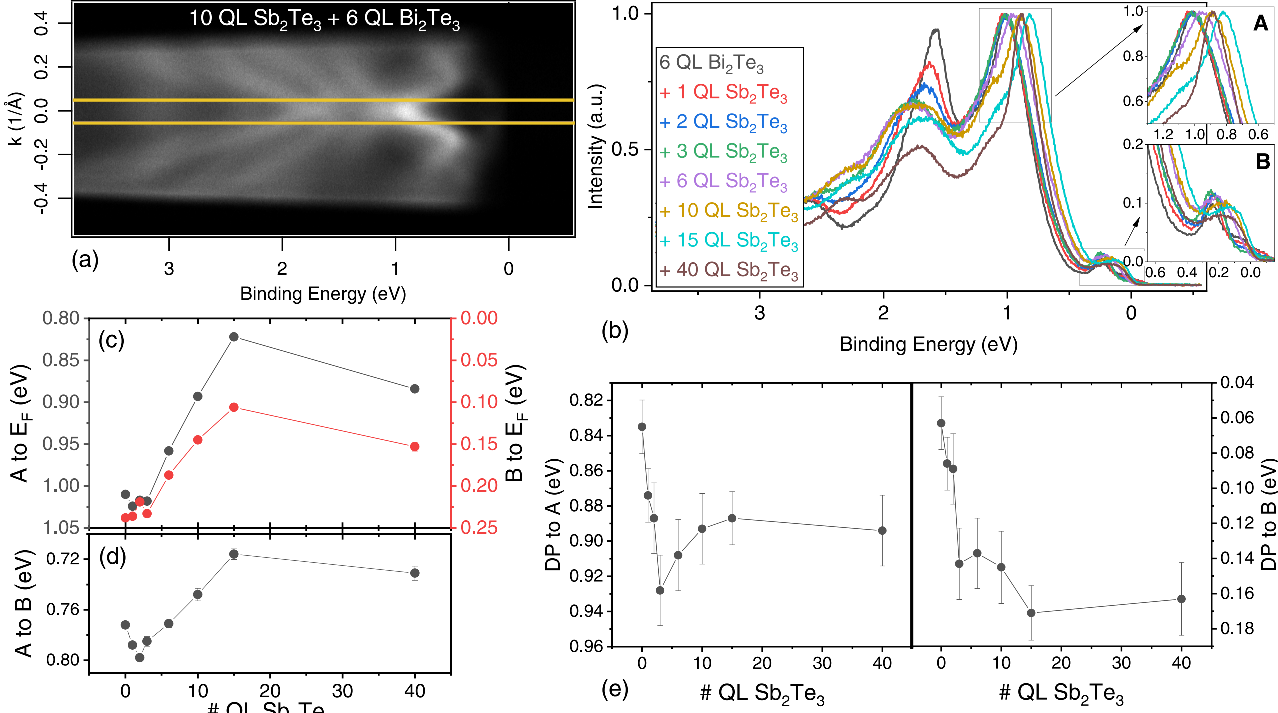

FIG. 3. (a) ARPES spectra of 10 QL Sb_2Te_3 grown at 220 °C on 6 QL Bi_2Te_3. (b) Energy distribution curves integrated over the area between the yellow lines in (a) for Sb_2Te_3 films—with thickness varying from 0 to 40 QLs—grown on top of 6 QLs of Bi_2Te_3. (c) Position of the features A (dark gray) and B (red) in relation to the Fermi level, varying with the thickness of the Sb_2Te_3 layer. (d) Position of feature A in relation to feature B for varying Sb_2Te_3 thickness. (e) Position of the Dirac point in relation to the features A (left) and B (right).

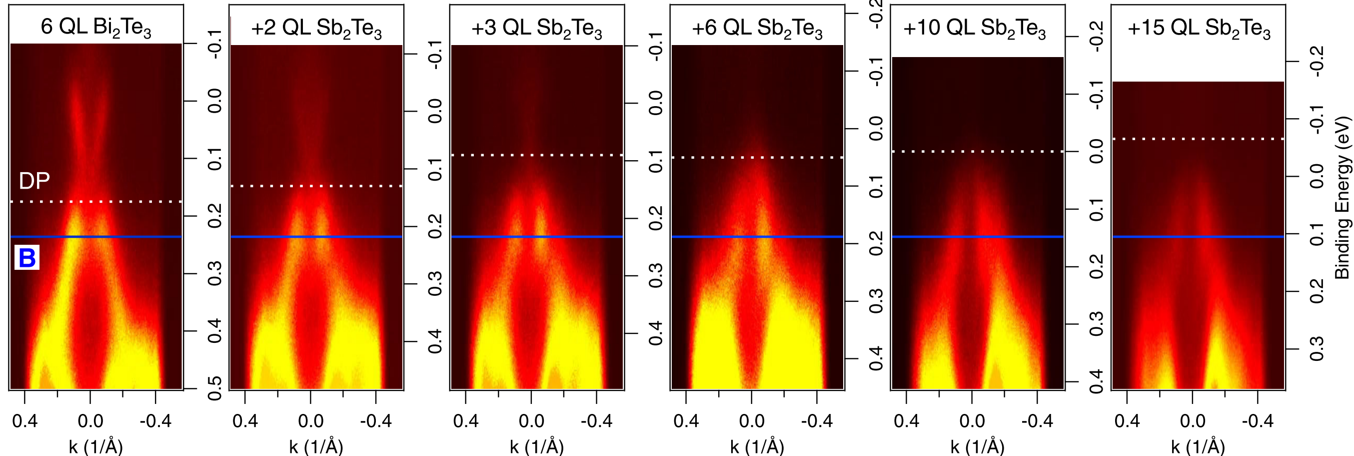

FIG. 4. ARPES results of Sb_2Te_3 grown on 6 QLs of Bi_2Te_3, showing the position of the Dirac point relative to the bulk feature B. The white dashed line indicates the position of the Dirac point (DP), and the blue line indicates the position of the feature B. All the spectra are aligned to the position of B.

the Sb_2Te_3 is dominating the bulk electronic structure of the heterostructure. For the intermediate Sb_2Te_3 thicknesses of 6–10 QLs, a gradual change between these two extremes is observed. Here, the bulk electronic structure comprises the relative Bi_2Te_3 and Sb_2Te_3 contributions.

To understand how the topological surface states are modified by the top TI layer, the position of the Dirac point was plotted relative to the bulk features A and B in Fig. 3(e), thus eliminating the effect of the chemical potential shift. The behavior is similar with respect to both features: the Dirac point shifts drastically (≈80–90 meV) when the thickness of the Sb_2Te_3 layer is between 1 and 3 QLs, and is then relatively constant [i.e., minor shifts of less than ≈30 meV that can be associated with the gradual changes of the bulk electronic structure shown in Fig. 3(d)] for thicker Sb_2Te_3 layers. These results are also visually represented in Fig. 4, where all the ARPES spectra were aligned to the position of the feature B. While the changes on the bulk features are gradual, the topological surface states change suddenly for 0–3 QLs of Sb_2Te_3. For pure Bi_2Te_3, the Dirac point is buried in the bulk valence band by ≈40–60 meV [18,26], and for 3 QL Sb_2Te_3 the Dirac point resides in the bulk band gap. In these heterostructures, the important changes in the topological surface states thus fully evolve during the deposition of only a few QLs of Sb_2Te_3 on the Bi_2Te_3, consistent with the calculations by Aramberri and Muñoz [20], which also studied the effect of strain.

Equally important is the fact that for these samples the Fermi level lies well above the bulk valence band and no bulk conduction band is visible in ARPES. This shift of the Dirac point in relation to the valence band, while keeping an insulating bulk, thus approximates these heterostructures to an idealized TI. Our results reveal that a direct access to the Dirac point by transport experiments can be facilitated via the growth of Sb_2Te_3/Bi_2Te_3 heterostructures, allowing for the measurement and use of the properties of the surfaces states only.

The composition of the heterostructures was investigated by XPS. Figure 5(a) shows the Te 4*d*, Sb 4*d*, and Bi 5*d* XPS spectra of 3 (green), 10 (violet), and 15 QL (dark gray) Sb_2Te_3 grown at 220 °C on Bi_2Te_3, and a Bi_2Te_3 spectrum as

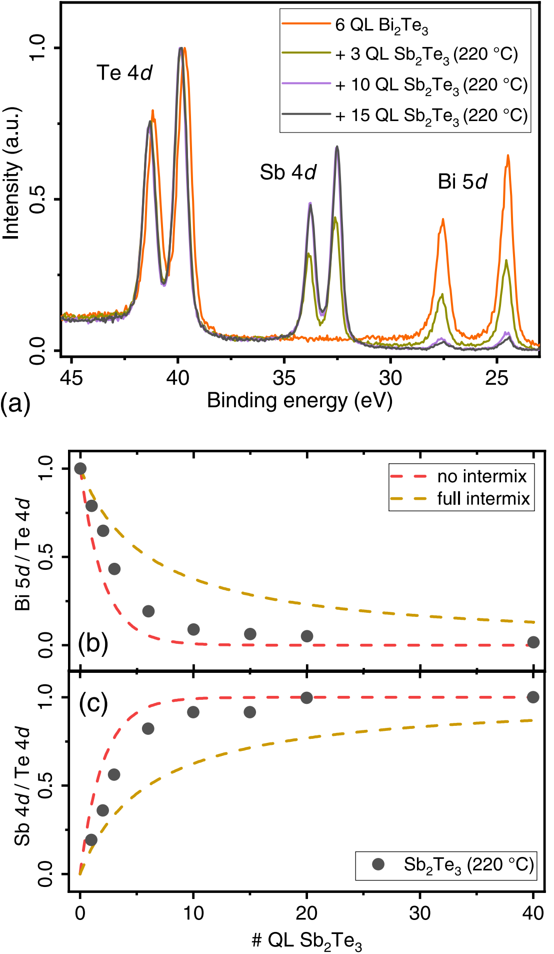

FIG. 5. (a) Te 4*d*, Sb 4*d*, and Bi 5*d* XPS spectra of 3 (green), 10 (violet), and 15 QL (dark gray) Sb_2Te_3 grown at 220 °C on top of 6 QL Bi_2Te_3 (orange). (b, c) Ratio of the integrated intensities corresponding to Bi 5*d* and Te 4*d* (b) and Sb 4*d* and Te 4*d* (c) for several thicknesses of the Sb_2Te_3 layer grown in the same conditions. The dashed lines represent the extreme cases where a sharp interface between the TIs (red) or a complete intermix between the TIs (yellow) exists.

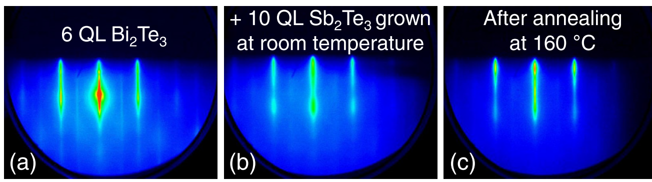

FIG. 6. RHEED patterns of (a) 6 QL Bi_2Te_3 on Al_2O_3 (0001), (b) 10 QLs of Sb_2Te_3 grown at room temperature on top of it, and (c) after annealing this heterostructure at 160 °C in Te atmosphere.

reference (orange). The spectra are normalized to the height of the Te $4d_{5/2}$ peak at about 40-eV binding energy. As the thickness of the Sb_2Te_3 layer increases, the Sb 4*d* signal increases and the Bi 5*d* signal decreases significantly. Nevertheless, for a thickness of 15 QLs, the Bi signal is still visible. Taking into consideration that the mean free path of photoelectrons created by 1486.6-eV x rays is about 1–2 nm, i.e., considerably smaller than the thickness of the Sb_2Te_3 layer, we would not expect any detectable Bi peak for the thicker Sb_2Te_3 layers. This could be explained by an intermixing between the Bi_2Te_3 and Sb_2Te_3 layers. Indeed, previous studies on TI heterostructures have reported that the interfaces are usually not sharp, and that some interdiffusion can be present [16,17,19]. Figure 5(b) shows the ratios of the Bi 5*d* and Te 4*d* integrated intensities for the various Sb_2Te_3 thicknesses. Details of the determination of the integrated intensities can be found in Appendix C. The two extreme cases of interaction between the layers are also represented: in red the case where no intermixing is present, and in yellow the case where the layers would intermix completely, giving rise to a homogeneous $(Bi_{1-x}Sb_x)_2Te_3$ layer. The curves were calculated based on the exponential behavior of the intensity at the surface resultant from a buried layer where we use a mean free path of 2 nm. The experimental data are between the two models, indicating that there exists indeed some diffusion between the TI layers. It should be noted that only for 40 QL Sb_2Te_3 the Bi 5*d* signal is almost completely suppressed. Figure 5(c) shows the ratios of the Sb 4*d* and Te 4*d* integrated intensities. The experimental data are also between the two represented models, corroborating the hypothesis of some diffusion between the layers.

B. Sb_2Te_3/Bi_2Te_3 heterostructures grown at room temperature

In order to minimize the interdiffusion between the TI layers, the growth procedure of the upper Sb_2Te_3 layer was altered. The films discussed in this section were grown at room temperature on top of 6 QL Bi_2Te_3. The Sb flux rate was kept at ≈0.5 Å/min, while the Te flux rate was now reduced to ≈0.9 Å/min, since we are no longer working in the Te distillation regime. The RHEED image of 10 QL Sb_2Te_3 grown in these conditions is shown in Fig. 6(b). The presence of streaks indicates that the growth of Sb_2Te_3, even at room temperature, is epitaxial and of acceptable quality. However, an increased background and broader streaks are also observable, indicating a poorer crystalline order in comparison to the film grown at 220 °C [Fig. 1(b)]. Subsequently, the film was annealed at 160 °C in Te atmosphere (flux rate ≈1.6 Å/min). The RHEED image in Fig. 6(c) shows now sharper streaks and a reduced background, indicating an improvement in the crystalline order of the Sb_2Te_3 layer.

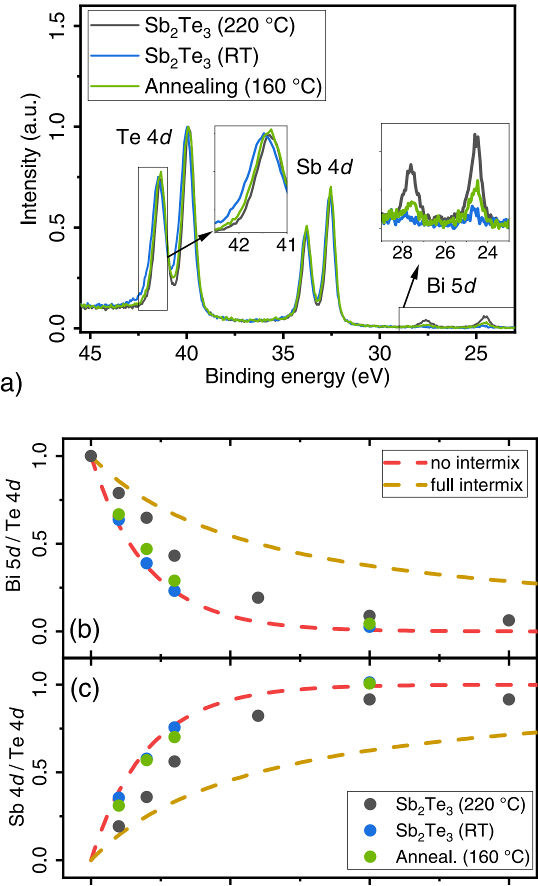

FIG. 7. (a) Te 4*d*, Sb 4*d*, and Bi 5*d* XPS spectra of 10 QL Sb_2Te_3—grown at 220 °C (dark gray) and at room temperature (RT) (blue)—on top of 6 QL Bi_2Te_3. The film grown at room temperature was subsequently annealed, and the spectrum is shown in green. (b), (c) Ratios of the integrated intensities corresponding to Bi 5*d* and Te 4*d* (b) and Sb 4*d* and Te 4*d* (c) for Sb_2Te_3 grown in the same conditions. The area of the Te 4*d* peaks was corrected for the excess elemental Te present for the growth at room temperature. The dashed lines represent the extreme cases where a sharp interface between the TIs (red) or a complete intermix between the TIs (yellow) exists.

XPS measurements were performed for all the films immediately after the growth at room temperature and also after the annealing procedure, in order to compare the differences in the diffusion at the interface of the heterostructures. Figure 7(a) shows the XPS spectra of 10 QL Sb_2Te_3 grown at room temperature in blue and after the annealing procedure in green. Additionally, the spectrum of the film grown at 220 °C is shown in dark gray as a reference. We can observe in the inset that the Bi 5*d* peaks are substantially reduced for the film grown at room temperature. After annealing, the intensity increases, but is still considerably lower than for the film grown at 220 °C. Furthermore, the line shape of the Te 4*d* peaks is altered, mainly for the film grown at room temperature. The shoulder present at higher binding energies can be attributed to some excess of elemental Te. The growth at room temperature makes the distillation method unviable and, consequently, the presence of some excess Te could not

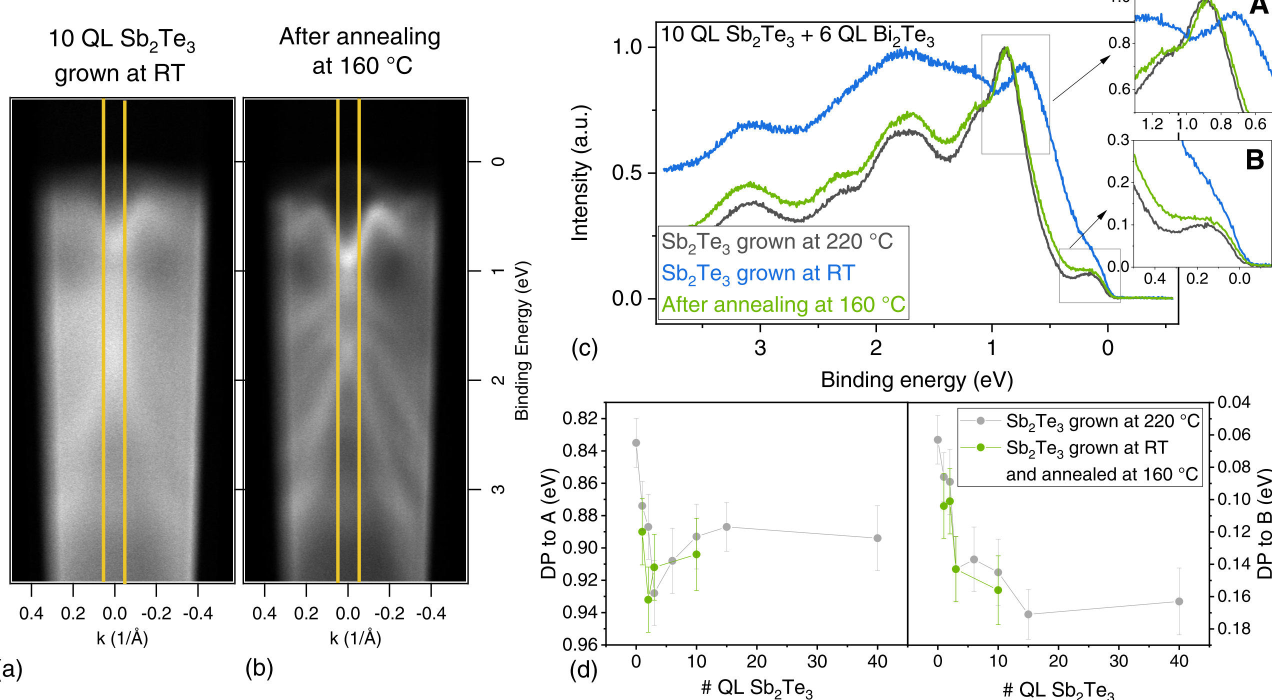

FIG. 8. (a) ARPES spectra of 10 QL Sb_2Te_3 grown at room temperature (RT) on 6 QL Bi_2Te_3. (b) ARPES spectra of the same film after annealing at 160 °C in Te atmosphere. (c) Energy distribution curves integrated over the area between the yellow lines in (a) (blue) and (b) (green). The curve for the film grown at 220 °C is depicted in dark gray for reference [also displayed in Fig. 3(b)]. (d) Position of the Dirac point in relation to the features A and B, varying with the thickness of the Sb_2Te_3 layer, for films grown at 220 °C (gray) and at room temperature, after the annealing process (green).

be completely avoided despite a careful optimization of the flux rates. After annealing, the line shape is much more similar to the films grown at 220 °C, indicating the removal of excess Te, although we have to note that a slight broadening at higher binding energies is still visible.

In Figs. 7(b) and 7(c) the ratios of Bi 5d/Te 4d and Sb 4d/Te 4d are displayed. For these, the integrated area corresponding to the Te 4d peaks was corrected to exclude the signal coming from elemental Te. The data for the films grown at 220 °C are shown in dark gray as a reference, as well as the two extreme models discussed in the previous section. The films grown at room temperature, shown in blue, follow very closely the model that describes a sharp interface. Thus, the growth of Sb_2Te_3 at room temperature substantially reduces the diffusion between the TI layers, allowing a sharper interface to form. Even after the annealing procedure, in green, we have considerably less intermixing than for the films grown at 220 °C.

To study potential differences in the band structure, ARPES measurements were performed after the growth at room temperature and after annealing. The results of a 10 QL Sb_2Te_3 film are shown in Figs. 8(a) and 8(b). The spectral features for the film grown at room temperature are quite blurred, reflecting the poorer crystalline quality of the film. In turn, after the annealing procedure, the background is noticeably reduced and the features are rather sharp, being comparable to those of the film grown at 220 °C [Fig. 3(a)]. The energy distribution curves in Fig. 8(c) show broad and ill-defined features for the film grown at room temperature, while after annealing they become sharper. Nevertheless, the broader features of the annealed film, in comparison to the one grown at higher temperature, may suggest some disorder left from the low-temperature growth. More importantly, the position of the features A and B remains nearly unaltered in comparison to the film grown at 220 °C, with a shift of only ≈20 meV to lower binding energies. This small difference might be caused by the suppressed interdiffusion between the TIs, and the resulting differences in doping.

Figure 8(d) illustrates the position of the Dirac point in relation to the features A and B. Similarly to what was described in the previous section, the position of the Dirac point changes appreciably for the very thin Sb_2Te_3 top layers and is rather constant for thicker layers, confirming once more that the relevant surface state engineering happens already for the initial Sb_2Te_3 layers. While the behavior of the larger Sb_2Te_3 thicknesses is comparable for both growth procedures, there are slight deviations for the thin heterostructures. For the 1 and 2 QL Sb_2Te_3 heterostructures, a larger shift of the Dirac point away from features A and B is observed for the films grown at room temperature. This can be understood considering the fact that there is less intermixing present in the heterostructures grown at low temperature and, thus, the character of Sb_2Te_3 is already more clearly visible for the very thin films. The overall comparable behavior of the heterostructures prepared in different conditions reinforces the argument that, by tracking the position of the Dirac point relative to bulk features, one can separate the effect of uncontrolled doping that otherwise will mask the results.

IV. CONCLUSIONS

In our *in situ* ARPES study, we systematically investigate the modulation of the topological surface states of MBE-grown Sb_2Te_3/Bi_2Te_3 heterostructures as a function of the Sb_2Te_3 adlayer thickness. For thin Sb_2Te_3 layers of about 1–3 QLs, the Dirac point is extracted from the bulk valence band into the bulk band gap, while for thicker Sb_2Te_3 layers the chemical potential shift prevails, shifting rigidly the entire valence band together with the surface states by up to $\approx$240 meV. Our results clearly show that the first 1–3 QLs of Sb_2Te_3 play the crucial role in the engineering of the topological surface states in the TI heterostructure. This yields important insights for the design of TI heterostructures with optimized topological insulator properties.

Additionally, we find that the diffusion between the topological insulator layers can be partly avoided when growing the top layer at room temperature, and the diffusion is suppressed even after a subsequent annealing. However, there is a compromise in the high quality of the samples as indicated by slightly broader ARPES features.

ACKNOWLEDGMENTS

The authors would like to thank S. Wirth for the valuable discussions and W.-H. Peng, K. Höfer, and C. Becker for the skillful technical assistance. We gratefully acknowledge financial support from the Deutsche Forschungsgemeinschaft through SPP Priority Program No. 1666 (“Topological Insulators”) and the Max Planck–POSTECH/Hsinchu Center for Complex Phase Materials. C.N.W. acknowledges support from the Ministry of Science and Technology of Taiwan, through Grant No. 105-2112-M-007-014-MY3, and V.M.P. acknowledges support from the International Max Planck Research School for Chemistry and Physics of Quantum Materials.

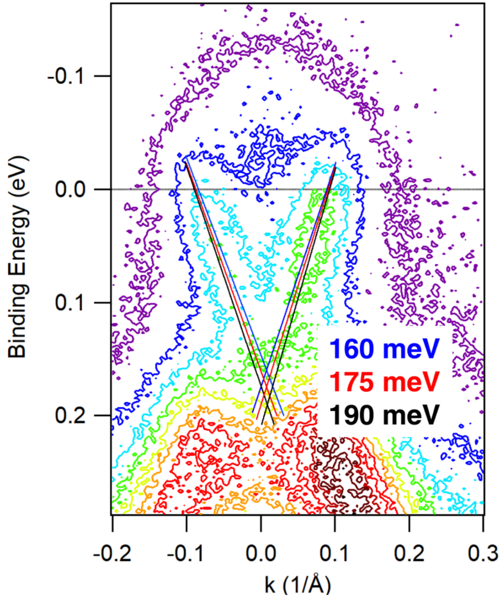

FIG. 9. ARPES contour plot of 6 QLs of Bi_2Te_3 used to determine the position of the Dirac point and the corresponding error bar.

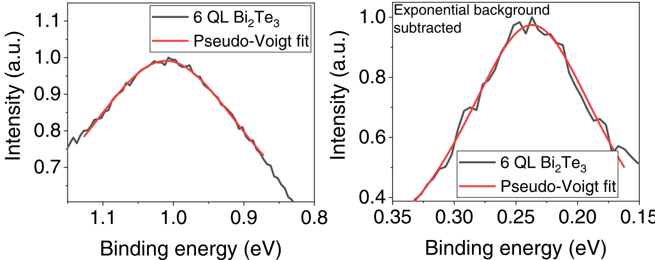

FIG. 10. Energy distribution curves near features A (left) and B (right) for a film with 6 QLs of Bi_2Te_3 and the respective pseudo-Voigt fits.

APPENDIX A: DETERMINATION OF THE DIRAC POINT

The determination of the Dirac point is exemplarily shown in Fig. 9 for a 6 QL Bi_2Te_3 film. The Dirac point is found by positioning straight lines (representing the Dirac cone) on the maxima of the contour lines of the topological surface states and then determining their crossing point. The error bar of the Dirac point is estimated from the variations in the energy of the crossing point of the straight lines upon varying the slope of the lines shown in blue, red, and black.

APPENDIX B: DETERMINATION OF PEAKS A AND B

Figure 10 shows the analysis of peaks A and B for a 6 QL Bi_2Te_3 film. The position of the features was obtained through pseudo-Voigt fits, shown in red. An exponential background was subtracted for the analysis of B. The error of the procedure was estimated by varying the fitting range within reasonable values.

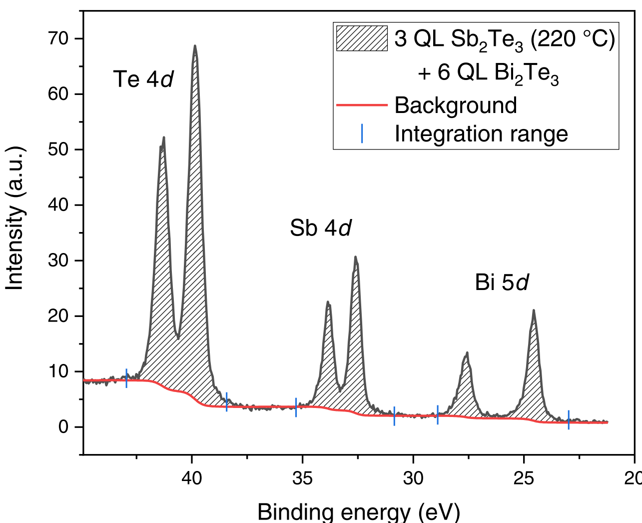

FIG. 11. XPS spectrum of 3 QLs of Sb_2Te_3 on 6 QLs of Bi_2Te_3, illustrating the method used for the determination of the Sb/Te and Bi/Te ratios.

APPENDIX C: DETERMINATION OF Sb/Te AND Bi/Te RATIOS

Figure 11 illustrates the XPS spectrum of the Te 4*d*, Sb 4*d*, and Bi 5*d* core levels for 3 QLs of Sb_2Te_3 on 6 QLs of Bi_2Te_3, showing in red the subtracted Shirley (integral-type) background. The integrated areas of each of the core levels were calculated for the shaded area in between the blue markers. The ratios discussed in Figs. 5(b), 5(c), 7(b), and 7(c) of the main text refer to the fraction of the integrated areas Bi 5*d*/Te 4*d* (b) and Sb 4*d*/Te 4*d* (c). The errors were estimated by varying the integration ranges (blue markers) and the parameters used to calculate the background (red curve). The error bars are not visible in the scales used in Figs. 5(b), 5(c), 7(b), and 7(c).

[1] L. Fu, C. L. Kane, and E. J. Mele, Phys. Rev. Lett. **98**, 106803 (2007).

[2] M. Z. Hasan and C. L. Kane, Rev. Mod. Phys. **82**, 3045 (2010).

[3] Y. Xia, D. Qian, D. Hsieh, L. Wray, A. Pal, H. Lin, A. Bansil, D. Grauer, Y. S. Hor, R. J. Cava, and M. Z. Hasan, Nat. Phys. **5**, 398 (2009).

[4] Y. L. Chen, J. G. Analytis, J.-H. Chu, Z. K. Liu, S.-K. Mo, X. L. Qi, H. J. Zhang, D. H. Lu, X. Dai, Z. Fang, S. C. Zhang, I. R. Fisher, Z. Hussain, and Z.-X. Shen, Science **325**, 178 (2009).

[5] D. Hsieh, Y. Xia, D. Qian, L. Wray, F. Meier, J. H. Dil, J. Osterwalder, L. Patthey, A. V. Fedorov, H. Lin, A. Bansil, D. Grauer, Y. S. Hor, R. J. Cava, and M. Z. Hasan, Phys. Rev. Lett. **103**, 146401 (2009).

[6] R. J. Cava, H. Ji, M. K. Fuccillo, Q. D. Gibson, and Y. S. Hor, J. Mater. Chem. C **1**, 3176 (2013).

[7] S. Zhu, Y. Ishida, K. Kuroda, K. Sumida, M. Ye, J. Wang, H. Pan, M. Taniguchi, S. Qiao, S. Shin, and A. Kimura, Sci. Rep. **5**, 13213 (2015).

[8] H. Zhang, C.-X. Liu, X.-L. Qi, X. Dai, Z. Fang, and S.-C. Zhang, Nat. Phys. **5**, 438 (2009).

[9] J. Zhang, C.-Z. Chang, Z. Zhang, J. Wen, X. Feng, K. Li, M. Liu, K. He, L. Wang, X. Chen, Q.-K. Xue, X. Ma, and Y. Wang, Nat. Commun. **2**, 574 (2011).

[10] D. Kong, Y. Chen, J. J. Cha, Q. Zhang, J. G. Analytis, K. Lai, Z. Liu, S. S. Hong, K. J. Koski, S.-K. Mo, Z. Hussain, I. R. Fisher, Z.-X. Shen, and Y. Cui, Nat. Nanotechnol. **6**, 705 (2011).

[11] T. Arakane, T. Sato, S. Souma, K. Kosaka, K. Nakayama, M. Komatsu, T. Takahashi, Z. Ren, K. Segawa, and Y. Ando, Nat. Commun. **3**, 636 (2012).

[12] X. He, T. Guan, X. Wang, B. Feng, P. Cheng, L. Chen, Y. Li, and K. Wu, Appl. Phys. Lett. **101**, 123111 (2012).

[13] J. Kellner, M. Eschbach, J. Kampmeier, M. Lanius, E. Młyńczak, G. Mussler, B. Holländer, L. Plucinski, M. Liebmann, D. Grützmacher, C. M. Schneider, and M. Morgenstern, Appl. Phys. Lett. **107**, 251603 (2015).

[14] C. Weyrich, M. Drögeler, J. Kampmeier, M. Eschbach, G. Mussler, T. Merzenich, T. Stoica, I. E. Batov, J. Schubert, L. Plucinski, B. Beschoten, C. M. Schneider, C. Stampfer, D. Grützmacher, and T. Schäpers, J. Phys.: Condens. Matter **28**, 495501 (2016).

[15] K. L. Scipioni, Z. Wang, Y. Maximenko, F. Katmis, C. Steiner, and V. Madhavan, Phys. Rev. B **97**, 125150 (2018).

[16] Z. Zhang, X. Feng, M. Guo, Y. Ou, J. Zhang, K. Li, L. Wang, X. Chen, Q. Xue, X. Ma, K. He, and Y. Wang, Phys. Status Solidi: Rapid Res. Lett. **7**, 142 (2013).

[17] M. Eschbach, E. Młyńczak, J. Kellner, J. Kampmeier, M. Lanius, E. Neumann, C. Weyrich, M. Gehlmann, P. Gospodarič, S. Döring, G. Mussler, N. Demarina, M. Luysberg, G. Bihlmayer, T. Schäpers, L. Plucinski, S. Blügel, M. Morgenstern, C. M. Schneider, and D. Grützmacher, Nat. Commun. **6**, 8816 (2015).

[18] C.-Z. Chang, P. Tang, X. Feng, K. Li, X.-C. Ma, W. Duan, K. He, and Q.-K. Xue, Phys. Rev. Lett. **115**, 136801 (2015).

[19] M. Lanius, J. Kampmeier, C. Weyrich, S. Kölling, M. Schall, P. Schüffelgen, E. Neumann, M. Luysberg, G. Mussler, P. M. Koenraad, T. Schäpers, and D. Grützmacher, Cryst. Growth Des. **16**, 2057 (2016).

[20] H. Aramberri and M. C. Muñoz, Phys. Rev. B **95**, 205422 (2017).

[21] V. M. Pereira, S. G. Altendorf, C. E. Liu, S. C. Liao, A. C. Komarek, M. Guo, H. J. Lin, C. T. Chen, M. Hong, J. Kwo, L. H. Tjeng, and C. N. Wu, Phys. Rev. Mater. **4**, 064202 (2020).

[22] V. M. Pereira, C. N. Wu, C.-A. Knight, A. Choa, L. H. Tjeng, and S. G. Altendorf, APL Mater. **8**, 071114 (2020).

[23] V. M. Pereira, C.-N. Wu, K. Höfer, A. Choa, C.-A. Knight, J. Swanson, C. Becker, A. C. Komarek, A. D. Rata, S. Rößler, S. Wirth, M. Guo, M. Hong, J. Kwo, L. H. Tjeng, and S. G. Altendorf, Phys. Status Solidi B **258**, 2000346 (2021).

[24] K. Höfer, C. Becker, D. Rata, J. Swanson, P. Thalmeier, and L. H. Tjeng, Proc. Natl. Acad. Sci. USA **111**, 14979 (2014).

[25] L. H. Tjeng, R. Hesper, A. C. L. Heessels, A. Heeres, H. T. Jonkman, and G. A. Sawatzky, Solid State Commun. **103**, 31 (1997).

[26] T. Förster, P. Krüger, and M. Rohlfing, Phys. Rev. B **93**, 205442 (2016).